Rowland, Kristopher John; Afshar Vahid, Shahraam; Monro, Tanya Mary.
Bandgaps and antiresonances in integrated-ARROWs and Bragg fibers; a simple model, *Optics Express*, 2008; 16(22):17935-17951.

http://hdl.handle.net/2440/51260

Bandgaps and antiresonances in integrated-ARROWs and Bragg fibers; a simple model

Kristopher J. Rowland, Shahraam Afshar V. and Tanya M. Monro

Centre of Expertise in Photonics, School of Chemistry & Physics, University of Adelaide, Australia, SA, 5005.

kristopher.rowland@adelaide.edu.au

http://www.physics.adelaide.edu.au/photonics

Abstract: We consider the spectral properties of dielectric waveguides with low refractive index cores and binary layered claddings, such as Bragg fibers and integrated-ARROWs. We show that the full, nontrivial, 2-D spectrum of Bloch bands (hence bandgaps) of such claddings correspond, in structure and topology, to the dispersion properties of both constituent layer types; quantitatively demonstrating an intimate relationship between the bandgap and antiresonance guidance mechanisms. The dispersion functions of these layers, and the interactions thereof, thus form what we coin the Stratified Planar Anti-Resonant Reflecting Optical Waveguide (SPARROW) model, capable of quantitative, analytic, descriptions of many nontrivial bandgap and antiresonance properties. The SPARROW model is useful for the spectral analysis and design of Bragg fibers and integrated-ARROWs with cores of arbitrary refractive index (equal to or less than the lowest cladding index). Both waveguide types are of interest for sensing and microfluidic applications due to their natural ability to guide light within low-index cores, permitting low-loss guidance within a large range of gases and liquids. A liquid-core Bragg fiber is discussed as an example, demonstrating the applicability of the SPARROW model to realistic and important waveguide designs.

References and links

1. P. Yeh, A. Yariv and C. Hong, "Electromagnetic propagation in periodic stratified media. I. General theory," J. Opt. Soc. Am. **67**, 423–438 (1977).
2. Y. Fink, D. J. Ripin, S. Fan, C. Chen, J. D. Joannopoulos, and E. L. Thomas, "Guiding optical light in air using an all-dielectric structure," J. Lightwave Technol. **19**, 2039–2041 (1999).
3. S. G. Johnson, M. Ibanescu, M. Skorobogatiy, O. Weisberg, T. Engeness, M. Soljačić, S. Jacobs, J. Joannopoulos, and Y. Fink, "Low-loss asymptotically single-mode propagation in large-core OmniGuide fibers," Opt. Express **9**, 748–779 (2001).
4. B. Temelkuran, S. D. Hart, G. Benoit, J. D. Joannopoulos, and Y. Fink, "Wavelength-scalable hollow optical fibres with large photonic bandgaps for CO2 laser transmission," Nature **420**, 650–653 (2002).
5. G. Vienne, Y. Xu, C. Jakobsen, H. Deyerl, J. Jensen, T. Sørensen, T. Hansen, Y. Huang, M. Terrel, R. Lee, N. Mortensen, J. Broeng, H. Simonsen, A. Bjarklev, and Amnon Yariv, "Ultra-large bandwidth hollow-core guiding in all-silica Bragg fibers with nano-supports," Opt. Express **12**, 3500–3508 (2004).

6. K. Kuriki, O. Shapira, S. D. Hart, G. Benoit, Y. Kuriki, J. F. Viens, M. Bayindir, J. D. Joannopoulos, and Y. Fink, "Hollow multilayer photonic bandgap fibers for NIR applications," Opt. Express **12**, 1510–1517 (2004).

7. T. Katagiri, Y. Matsuura, and M. Miyagi, "Photonic bandgap fiber with a silica core and multilayer dielectric cladding," Opt. Lett. **29**, 557–559 (2004).

8. T. Katagiri, Y. Matsuura, and M. Miyagi, "All-solid single-mode bragg fibers for compact fiber devices," J. Lightwave Technol. **24**, 4314–4318 (2006).

9. J. L. Archambault, R. J. Black, S. Lacroix, and J. Bures, "Loss calculations for antiresonant waveguides," J. Lightwave Technol. **11**, 416–423 (1993).

10. D. Yin, J.P. Barber, A. R. Hawkins, and H. Schmidt, "Waveguide loss optimization in hollow-core ARROW waveguides," Opt. Express **13**, 9331–9336 (2005).

11. D. Yin, H. Schmidt, J. P. Barber, E. J. Lunt, and A. R. Hawkins, "Optical characterisation of arch-shaped ARROW waveguides with liquid cores," Opt. Express **13**, 10564–10570 (2005).

12. F. Poli, M. Foroni, A. Cucinotta, and S. Selleri, "Spectral behavior of integrated antiresonant reflecting hollow-core waveguides," J. Lightwave Technol. **25**, 2599–2604 (2007).

13. H. Schmidt and A. R. Hawkins, "Optofluidic waveguides: I. Concepts and implementations," Microfluid. Nanofluid. **4**, 3–16 (2008).

14. Y. Fink, J. N. Winn, S. Fan, C. Chen, J. Michel, J. D. Joannopoulos, and E. L. Thomas, "A dielectric omnidirectional reflector," Science **282**, 1679–1682 (1998).

15. M. A. Duguay, Y. Kokubun, T. L. Koch, and L. Pfeiffer, "Antiresonant reflecting optical waveguides in $SiO_2 - Si$ multilayer structures," Appl. Phys. Lett. **49**, 13–15 (1986).

16. T. Baba and Y. Kokubun, "High efficiency light coupling from antiresonant reflecting optical waveguide to integrated photodetector using an antireflecting layer," Appl. Opt. **29**, 2781–2792 (1990).

17. T. Baba and Y. Kokubun, "Dispersion and radiations loss characteristics of antiresonant reflecting optical waveguides - numerical results and analytical expressions," J. Quantum Electron. **28**, 1689–1700 (1992).

18. A. K. Abeeluck, N. M. Litchinitser, C. Headley, and B. J. Eggleton, "Analysis of spectral characteristics of photonic bandgap waveguides," Opt. Express **10**, 1320–1333 (2002).

19. N. M. Litchinitser, A. K. Abeeluck, C. Headley, and B. J. Eggleton, "Antiresonant reflecting photonic crystal optical waveguides," Opt. Lett. **27**, 1592–1594 (2002).

20. N. M. Litchinitser, S. C. Dunn, B. Usner, B. J. Eggleton, T. P. White, R. C. McPhedran, and C. M. de Sterke, "Resonances in microstructured optical waveguides," Opt. Express **11**, 1243–1251 (2003).

21. N. M.Litchinitser, S. C. Dunn, P. E. Steinvurzel, B. J. Eggleton, T. P. White, R. C. McPhedran, and C. M. de Sterke, "Application of an ARROW model for designing tunable photonic devices," Opt. Express **12**, 1540–1550 (2004).

22. D. Yin, H. Schmidt, J. P. Barber, and A. R. Hawkins, "Integrated ARROW waveguides with hollow cores," Opt. Express **12**, 2710–2715 (2004).

23. K. J. Rowland, S. Afshar V., and T. M. Monro, "Novel low-loss bandgaps in all-silica Bragg fibers," J. Lightwave Technol. **26**, 43–51 (2008).

24. F. Poli, M. Foroni, D. Giovanelli, A. Cucinotta, S. Selleri, J. B. Jensen, J. Læsgaard, A. Bjarklev, G. Vienne, C. Jakobsen, and J. Broeng, "Silica bridge impact on hollow-core Bragg fiber transmission properties," Proceedings OFC 2007 (Anaheim, California), paper OML8 (2007).

25. T. A. Birks, G. J. Pearce, and D. M. Bird, "Approximate band structure calculation for photonic bandgap fibres," Opt. Express **14**, 9483–9490 (2006).

26. J. J. Hu, G. Ren, P. Shum, X. Yu, G. Wang, and C. Lu, "Analytical method for band structure calculation of photonic crystal fibers filled with liquid," Opt. Express **16**, 6668–6674 (2008).

27. J. A. Buck, *Fundamentals of Optical Fibers* (2nd ed., John Wiley & Sons, Inc., 2004).

28. M. Born and E. Wolf, *Principles of Optics* (7th ed., Cambridge University Press, 2002).

29. I. M. Bassett and A. Argyros, "Elimination of polarization degeneracy in round waveguides," Opt. Express **10**, 1342–1346 (2002).

30. A. Argyros, "Guided modes and loss in Bragg fibres," Opt. Express **10**, 1411–1417 (2002).

31. J. P. Barber, D. B. Conkey, M. M. Smith, J. R. Lee, B. A. Peeni, Z. A. George, A. R. Hawkins, D. Yin, and H. Schmidt, "Hollow waveguides on planar substrates with selectable geometry cores," Proceedings CLEO 2005 (San José, California), paper CTuD4 (2005).

32. P. K. Tien, "Light waves in thin films and integrated optics," Appl. Opt. **10**, 2395–2413 (1971).

33. P. Viale, S. Février, F Gérôme, and H. Vilard, "Confinement loss computation in photonic crystal fibres using a novel perfectly matched layer design," Proceedings of the COMSOL Multiphysics user's conference (Paris, 2005).

34. V. Finazzi, T. M. Monro, and D. J. Richardson, "Small-core silica holey fibers: nonlinearity and confinement loss trade-offs," J. Opt. Soc. Am. B **20**, 1427–1436 (2003).

35. J. Li and K. S. Chiang, "Disappearance of modes in planar Bragg waveguides," Opt. Lett. **32**, 2369–2371 (2007).

1. Introduction

This work focuses on two primary themes: the reconciliation of the bandgap and antiresonance guidance mechanisms for dielectric waveguides with cores of low refractive index and binary layered claddings (such as Fig. 1); and, from this, the construction of a simple analytic model for the analysis of the full, nontrivial, 2-D bandgap spectra of such cladding structures.
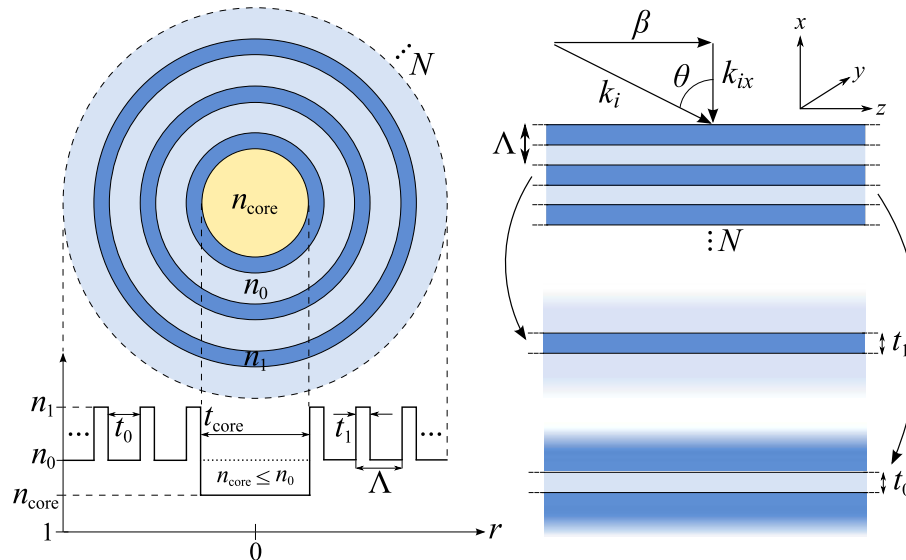

Fig. 1. Schematic representations of the fiber, stack and slab geometries discussed here. **Left**: An arbitrary Bragg fiber geometry. All parameters defined within. Refractive indices take any value such that $n_1 > n_0 \geq n_{core} \geq 1$. **Right**: The equivalent planar slab representation of the Bragg-cladding with the equivalent isolated constituent layers shown below. The vector diagram represents the decomposition of an incident ray's wavevector.

Considering the first theme, fibers with a binary-layered (Bragg) cladding are well known for their ability to confine light to cores with refractive indices equal to or lower than either of the cladding indices [1-8]. Analogous types of planar waveguides known as integrated Antiresonant Reflecting Optical Waveguides (integrated-ARROWs) exhibit similar low-index confinement behaviour [9-13] but are typically treated as distinct to Bragg waveguides and their associated bandgap guidance mechanism. The cladding of a Bragg waveguide is usually considered as a 1-D photonic crystal such that the behaviour of the resultant Bloch modes dictates whether light can or cannot couple to the cladding [1, 14]; core modes exist only for wavelengths and propagation constants that fall within the Bloch modes' forbidden regions (bandgaps). AR-ROW guidance, on the other hand, is attributed to the antiresonance of light with the individual cladding layers [9, 15]; a particular layer will preferentially guide light at its resonant frequencies such that the transverse component of the light interferes constructively with itself for each round trip. Thus, light sufficiently far from the cladding resonances will be confined to the core due to restricted coupling (antiresonance) with the cladding layers themselves.

Here we suggest that the distinction between Bragg-cladding waveguides and integrated-ARROWs is somewhat artificial, with the only difference being semantic: whether the cladding is periodic (multiple unit cells: 'Bragg') or not (single unit cell: 'ARROW'). Indeed, with hollow-core integrated-ARROWs now being considered with more than one binary cladding unit cell [10-12], this distinction ceases to exist. Thus, since these two waveguide structures are essentially the same, it is natural to expect a strong relationship between the bandgap and

antiresonance guidance mechanisms themselves. We explore this idea within by analysing the two approaches and directly comparing the results.

It is useful here to spell out an important misnomer regarding the use of the term 'ARROW'. As it was initially conceived, the model used to describe ARROWs typically assumed that one of the cladding layer refractive indices was much greater than the core and remaining cladding index [15]. As such, many ARROW designs have a core index *equal* to the lowest of the cladding indices [15-21]; we will call these *level-core* waveguides. Indeed, this line of thought saw the ARROW model successfully applied to (non-layered cladding) photonic crystal fibers (PCFs) [20, 21] and has spawned much interest in what have been termed 'ARROW-fibers': PCFs of a low-index substrate with a cladding of high-index rods (typically on, but not restricted to, a hexagonal lattice). It is implicitly assumed that such fibers have a core refractive index equal to the surrounding low-index substrate, just like the early (level-core) ARROWs; rightly so, since it is structurally the only possibility for a 2-D lattice based cladding as opposed to a layered one. For level-core waveguides, the predominant antiresonance behaviour comes from the high-index inclusions alone, with little dependence on their spacing [19]. However, the general definition of an ARROW by Archambault et al. [9] dictates that the core index can have *any value up to* that of the lowest cladding index; we will call these *depressed-core* waveguides. *All* cladding layer resonances in depressed-core waveguides influence the spectral behaviour of the core modes [9], not just the high-index layer resonances. Indeed, it is the Archambault-ARROW model that is considered for most current work on integrated hollow-core ARROWs [10, 11]. We believe this disparity between the use of the general Archambault-ARROW model and its restricted, Duguay-ARROW-based [15], form as applied to PCFs (the 'ARROW-fibers') [18-21] is responsible for the apparent bifurcation of the use of the ARROW principle in the integrated-waveguide and fiber fields. This is most clearly demonstrated (to the best of the Authors' knowledge) by the absence of antiresonance analyses for hollow-core Bragg fibers and the absence of a Bloch analysis for hollow-core integrated-ARROWs; the two waveguide structures being fundamentally similar (depressed core, binary layered cladding), as discussed. The work presented here clearly demonstrates how both the antiresonance and bandgap principles are applicable to any depressed-core waveguide with a binary stratified cladding, particularly for fibers and integrated waveguides respectively.

Within, we develop a generalised version of the Archambault-ARROW model and use it to demonstrate an intimate relationship between the bandgap and antiresonance guidance mechanisms associated with stratified cladding waveguides. We coin this new model the *Stratified Planar* Anti-Resonant Reflecting Optical Waveguide (SPARROW) model to distinguish it from both the original Archambault-ARROW model itself [9] and, in particular, the more restrictive level-core ARROW and (non-stratified) PCF applications based on the Duguay-ARROW model [15, 19-21]. Indeed, as will be shown later (Section 4.3), the Duguay-ARROW model is a special case of the SPARROW model (found by enforcing a level-core index profile). Further, we will demonstrate how all (both high- and low-index) cladding layer resonances must be considered together for the most general waveguide analysis and design, rather than considering them separately as is typically done via the Archambault-ARROW model [9, 10, 22].

For our second theme, it has recently been shown [23] that in single-material Bragg fibers [5, 23, 24] (hollow level-core waveguides) a new class of large bandwidth bandgaps are available, hence also available to any level-core layered-cladding waveguide (Fig. 1). This analysis also demonstrated that such cladding structures produce bandgap spectra with rich 2-D (effective mode index vs. frequency) structure below the light-line of the lowest-index cladding layer [23]. These gaps are distinct from, yet related to, the gaps typically studied in more conventional hollow-core solid-cladding Bragg fibers [3, 4, 6] which lie far from the low-index light-line. However, modelling of microstructured waveguides typically relies heavily on (often

cumbersome) numerical analyses of the full 2-D waveguide structures to determine the bandgap characteristics, highlighting the need for simpler models. While a Bloch-wave analysis may be used (and is throughout this work) on 1-D approximations to the cladding of a Bragg-cladding waveguide [1, 3-6, 14, 23], it is difficult to use the resultant semi-analytic bandgap condition [1] to glean direct physical insight into the relationship between the cladding parameters and the bandgap spectra's structure and topology. Semi-analytic models for the approximate calculation of band-edges have been derived for PCFs with a cladding of high-index rods [25, 26], but such approaches aren't suitable for depressed-core layered-cladding waveguides since the low-index layers are equally important [9].

Here we examine the resonances of the individual cladding layers, via the SPARROW model, to present an analytical physical description of these nontrivial bandgap properties. We demonstrate how our model can determine a number of nontrivial properties with simple, fully analytic, expressions. Such tools are indispensable for the understanding and design of depressed-core layered-cladding waveguides, whether they be fibers (multi-dielectric, such as the aforementioned hollow-core Bragg fibers [3, 4, 6], or single-material Bragg fibers [5, 23, 24]) or integrated-ARROWs [9-13]. We thus expect that the SPARROW model will be particularly useful for the design of layered-cladding waveguides with gas or liquid cores for applications in sensing, microfluidics, and novel nonlinear waveguides.

To give an overview, we begin with the relevant background theory on bandgaps and antiresonances in 1-D structures in Sections 2.1 and 2.2, respectively. The dispersion characteristics of high- and low-index slab waveguides are discussed in Section 2.3 and are used to formally define the Stratified Planar Anti-Resonant Reflecting Optical Waveguide model in Section 3. The expressions fundamental to the SPARROW model are the dispersion curves of the cladding layers considered in isolation (Section 2.3), giving the wavelengths and modal effective indices at which light preferentially couples to the cladding (resonances); avoiding these cladding resonances decreases the core-mode loss (antiresonance). The models ability to predict high- and low-loss wavelengths is confirmed via a numerical example in Section 3.1 where it is made clear that *both* the high- and low-index layer resonances must be taken into account in order to describe the chosen region of the 2-D bandgap spectrum. This follows directly from the definition of the *general antiresonance point* (Section 4.2) which explicitly accommodates this behaviour. As mentioned, further analysis of the curve interactions (Section 4) leads to expressions describing nontrivial properties of the associated bandgaps, such as: the positions of all bandgap closure points and, from them, a consistent nomenclature for arbitrary bandgap spectra (Section 4.1); the *central gap point* (Section 4.4) - a special case of the general antiresonance point; and a quantitative measure of the topology of arbitrary bandgap spectra - the number of gaps within a specific domain (Section 4.5). Concluding remarks are given in Section 5.

2. Background theory

2.1. Bragg stack Bloch analysis

It is well known that the bandgap properties of the cladding of a Bragg fiber can be well approximated by those of a planar Bragg stack [1, 3-6, 23]. Consider a Bragg fiber with cladding layer refractive indices n_1 and n_0 and core refractive index n_{core}, such that $n_1 > n_0 \geq n_{core} \geq 1$ (a 'depressed-core' waveguide as defined above), with layer thicknesses t_1 and t_0 and core thickness t_{core}, Fig. 1.

The work of Yeh et al. [1] derives a semi-analytic condition for the propagation conditions of light within an infinite periodic dielectric stack (infinite in the x and y dimensions with the number of layers $N \rightarrow \infty$, Fig. 1). An incident plane wave's wavevector ($\mathbf{k}_i = k_i \hat{\mathbf{k}}$ where $k_i = n_i k$ and $k = 2\pi/\lambda$) can be decomposed into normal ($k_{ix}\hat{\mathbf{x}}$) and planar components ($\beta \hat{\mathbf{z}}$), Fig. 1. Care should be taken not to confuse the free space wavenumber k and the 0th layer type's wavevector

amplitude $k_0 = n_0 k$. β is thus related to the propagation constant of the composite waveguide. Hereon we will more often refer to the effective modal refractive index $\tilde{n} = \beta / k$. k_{ix} corresponds to plane waves propagating normal to the stack (due to transmission and reflection between layers), where the index i specifies what layer type the plane wave is in ($i \in \{0, 1\}$). It follows that $k_{ix} = \{k_i^2 - \beta^2\}^{\frac{1}{2}} = k\{n_i - \tilde{n}\}^{\frac{1}{2}}$.

Two matrix recursion relations, describing transverse electric (TE) or transverse magnetic (TM) waves, can be derived via the Bloch-Floquet theorem, relating plane waves in the stack to an incident plane wave [1]. The resultant 2×2 Bloch-wave eigenvalue equation has only one unique matrix element, $A_{TE,TM}(k, \tilde{n})$ [1], which is a function only of the layer parameters (n_i and t_i) and wave parameters (k and $\tilde{n}$). Only solutions satisfying the condition [1]:

$$|\text{Re}\{A_{TE,TM}(k, \tilde{n})\}| < 1, \tag{1}$$

correspond to (non-evanescent) waves allowed to propagate perpendicular to the Bragg stack (the x-direction in Fig. 1). The evaluation of Inequality 1 for a particular layer configuration is straightforward since k and $\tilde{n}$ are the only free parameters. The regions in the 2-dimensional space $(k, \tilde{n})$ satisfying Ineq. (1) are allowed bands (waves allowed to propagate in the cladding) for either TE or TM waves (in Fig. 2, black represents where the TE and TM bands overlap, so for $\tilde{n} < n_0$ all TE bands are black since the TM bands are larger, thus both black and grey). For $\tilde{n} > n_0$ the TE and TM bands diverge [1], Fig. 2. The regions in between the allowed bands are the bandgaps. Thus, any core mode of a depressed-core waveguide ($1 \leq n_{core} \leq n_0$) must have both k and $\tilde{n}$ within a bandgap. All figures within plot over $(\Lambda/\lambda, \tilde{n}) = (\Lambda k / 2\pi, \tilde{n})$ so that both axes are unitless, naturally representing the scale-invariance of the system.
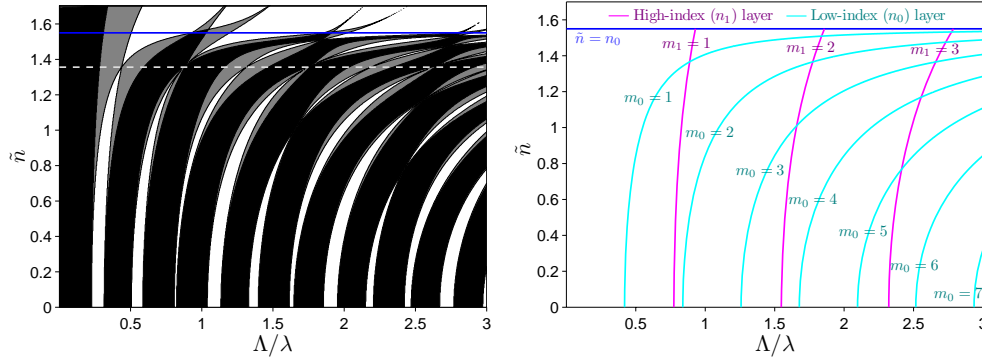

Fig. 2. **Left**: A bandgap map generated via the Bloch theorem (Section 2.1) for a Bragg fiber cladding like that considered in [4]: $t_1 = 0.27\mu m$, $t_0 = 0.9\mu m$, $n_1 = 2.8$ and $n_0 = 1.55$. *Color scheme* (for $\tilde{n} < n_0$): as described in text, Section 2.1; black for TE bands, black and grey for TM bands ($\Rightarrow$ white for TM bandgaps, white and grey for TE bandgaps). *Solid blue line*: the n_0-light-line. *Dotted line*: the Brewster line, $\tilde{n} = n_B$. **Right**: A plot of all the SPARROW curves (dispersion curves of the equivalent isolated layers), via Eq. (6), for the same cladding and bandgap domain. *Magenta*: high-index (n_1) layer, $\tilde{n}_{m_1}(k)$. *Cyan*: low-index (n_0) layer, $\tilde{n}_{m_0}(k)$.

From Fig. 1, glancing incidence ($\theta = \pi/2$) produces $\beta = k_i \Rightarrow \tilde{n} = n_i$, referred to as the '$n_i$-light-line'. For waveguides of sufficiently large core radius, core-bound modes of low order exhibit dispersion curves $\tilde{n}(k)$ close to those of plane waves of glancing incidence, hence $\tilde{n}(k) \approx n_i$. Core modes of the waveguides considered here will thus typically only exist where the n_{core}-light-line intercepts the relevant bandgap; namely, TE modes within TE gaps and TM and HE modes within TM gaps (since HE modes contain components of both TE and TM rays [27]).

As demonstrated in Fig. 2, the TM bandgaps close up at a specific value of $n_B = n_1 n_0 / \sqrt{n_1^2 + n_0^2}$ due to the well known Brewster phenomenon [28-30], where TM rays satisfying the Brewster condition are totally transmitted thus preventing the existence of a bandgap at that specific value of $\tilde{n}$ [30]. Thus, for $\tilde{n} < n_0$, the TM gaps always lie within the TE gaps [23]. The closure of the TE gaps close to n_B in the case of Fig. 2 is coincidental (discussed further in Sections 3 and 4.1).

Figure 2 shows the bandgap map of the layered cladding considered in [4]. In particular, note the nontrivial bandgap structure below the n_0-light-line, as recently discussed in [23]. As mentioned earlier, it is the characteristics of this rich structure that we seek to explain via the SPARROW model. It is worth noting here that analyses of Bragg fibers thus far have typically only dealt with two main regions of the bandgap spectrum: the region close to $\tilde{n} = 0$, as is the case for conventional Bragg fibers [3, 4, 6, 23], and the region near $\tilde{n} = n_0$, as is the case for the more recently discussed types of single-material Bragg fibers [5, 23] (and also the level-core silicon/silica Bragg fibers of [7, 8]). The complex bandgap structure that lies between these two regions becomes increasingly important as the filling of hollow waveguides becomes more fruitful [10, 11, 13, 22] and such waveguides begin to vary in core sizes and shapes [10, 11, 13, 22-24, 31]; low-order modes within large cores will tend to exhibit $\tilde{n} \approx n_{core}$ [27] and will move to lower $\tilde{n}$ as the core size decreases (e.g. [23]); higher-order modes also naturally exhibit lower $\tilde{n}$ and hence intercept different bandgap regions (important for exploiting modal-loss discrimination [3, 23, 29, 30]). More precisely, by changing n_{core} or t_{core}, the confined modes' $\tilde{n}$ will be able to intercept this richly structured bandgap region, making analyses based on the SPARROW model increasingly important. An explicit example of a liquid-core Bragg fiber is presented in Section 3.1.

2.2. ARROW models

Originally discussed in the context of planar waveguides with a single high-index cladding layer in 1986 [15], the Anti-Resonant Reflecting Optical Waveguide (ARROW) model of Duguay et al. demonstrated how light could be confined to a low-index core by inhibited coupling (antiresonance) with a high-index cladding layer. In 1994, this model was later generalised to arbitrary numbers of cladding layers with arbitrary refractive indices by Archambault et al. [9]. The only restriction for core-guidance in the Archambault-ARROW model was that the core must have a refractive index equal to or less than the lowest of the cladding indices: $n_{core} \leq \min\{n_i\}$. By considering the transverse phase accumulated by a propagating ray (Fig. 1) per round trip (*including* that from traversing the core, via the V-parameter) and equating it to 2π (resonance), the Archambault-ARROW model determines the wavelengths at which the ith cladding layer will be resonant with the guided light [9, 22]:

$$\lambda_{m_i} = \frac{2t_i}{m_i} \sqrt{n_i^2 - n_{core}^2 + \left(\frac{U_\infty \lambda}{2\pi t_{core}} \right)^2}, \tag{2}$$

where $m_i \in \mathbb{Z}^+$ is the resonance order of the ith layer type and U_∞ takes the value $(p+1)\pi/2$ for a planar core, with mode order $p \in \mathbb{Z}^+$, or value $j_{\nu\mu}$, with azimuthal and radial mode orders μ and ν respectively (such that the νth-order Bessel function satisfies $J_\nu(j_{\nu\mu}) = 0$), for a cylindrical core. Note how in Eq. (2) the properties of the core are incorporated into the resonance conditions by default (via n_{core}, t_{core} and U_∞). In the SPARROW model we define below, the resonance analysis is completely decoupled from all core properties, being related to them (importantly) only via the effective mode index $\tilde{n}$. Considering the individual layers' full dispersion curves permits a mode-coupling (core to cladding) type analysis: the closer a core mode's $\tilde{n}$ lies to those of the cladding layers, the stronger the coupling to the cladding,

producing a larger core-mode confinement loss (CL).

From Eq. (2), the wavelengths producing antiresonance with *individual* cladding layers are found between the cladding layer resonance points by considering half-integer layer mode orders: $m_i \rightarrow m_i + \frac{1}{2}$ [9]. Using this approach, the Archambault-ARROW model has recently been applied successfully to depressed-core gas- and liquid-filled hollow-core integrated-ARROW waveguides [10, 11, 22] but tends to be used to achieve antiresonance with each cladding layer individually and only for $m_i = 1$ (e.g. [22]). While this approach is sufficient for designing a guidance regime, the tuning of each layer separately is unnecessarily restrictive (and potentially produces a higher confinement loss than desired by bringing the resonances of both layer types, rather than just one, close to the k of interest). As will be shown in Section 4.2, a general analysis requires the resonances of all layer types to be considered together, leading to our definition of the *general antiresonance point* k_c' which is more suited for general analyses of arbitrary cladding configurations and strictly necessary for arbitrary $\tilde{n}$ and m_i.

By substituting $U_\infty \rightarrow \pi/2$ (planar core with $p = 0$) in Eq. (2), the Duguay-ARROW resonance condition [15] is derived (where only one, high-index, cladding layer type is considered, making the i label redundant). This substitution is equivalent to assuming the core-bound rays only make glancing incidence with the cladding layer [15]. The Duguay-ARROW model has been successfully applied to different types of level-core ($n_{core} = n_0 < n_1$) ARROWs (e.g. [15-17]). More recently, the Duguay-ARROW model has also been employed by Litchinitser et al. [19-21] and Abeeluck et al. [18] to describe antiresonance guidance in photonic crystal fibers (PCFs) in the large-core regime, including level-core Bragg fibers [19], and, in particular, PCFs with a cladding of high-index rods [20, 21]. For stratified claddings, the large-core limit reduces the cladding layer resonance condition to [19]:

$$\lambda_m = \frac{2t_1}{m} \sqrt{n_1^2 - n_0^2}. \tag{3}$$

Incidentally, note that $m \rightarrow m + \frac{1}{2}$ is required for the rod-cladding case, to accommodate for the modal cut-off frequencies of cylinders instead of layers [20, 21]. One important property of these level-core ($n_{core} = n_0$) waveguides is that the resonance effects of the cladding on the core-guided modes is dominated by the high-index inclusions, independent of the low-index region between them [19]. This phenomena is quantitatively explained (for layered claddings) in Section 4.3 by setting $\tilde{n} = n_{core} = n_0$ in the SPARROW model.

While level-core Bragg fibers have been discussed in the context of the Duguay-ARROW model [18, 19], the more general Archambault-ARROW model appears to be absent from analyses of solid-cladding hollow-core ($n_0 > n_{core} = 1$) Bragg fibers, where Bloch-wave analysis (as in Section 2.1) is more common [1, 3-6, 23]. Likewise, the analysis of multilayer hollow-core integrated-ARROWs [9-13] appears to primarily use the Archambault-ARROW model, foregoing a Bloch-wave analysis. By demonstrating the intimate relationship between the bandgap and antiresonance guidance mechanisms here, we hope that the artificial bifurcation of these techniques is overcome.

As shown in the next section, the SPARROW model is essentially a modified version of the Archambault-ARROW model where we decouple the core properties from the cladding layer resonances (without enforcing a large-core regime). The resonance conditions are instead expressed as individual layer dispersion relations in terms of a general modal refractive index $\tilde{n}$. This then permits a bandgap-style analysis of the layer resonances (Section 3) ultimately showing a close relationship between the bandgap and antiresonance guidance mechanisms and, more importantly, also allowing the derivation of some very simple expressions for nontrivial and useful properties of arbitrary bandgap spectra (Section 4).

2.3. Dispersion analysis of slab waveguides below the light-line

Consider now the layers that constitute a Bragg stack, each in isolation (represented in the bottom-right of Fig. 1). Let the isolated slab and its surrounding cladding have refractive indices n_a and n_b, respectively. There are thus two types of slab waveguide to consider: one with a high slab index $n_a = n_1$ with a lower cladding index $n_b = n_0$ ($n_a > n_b$), and one with a low slab index $n_a = n_0$ with a high cladding index $n_b = n_1$ ($n_a < n_b$); $n_1 > n_0$ as before (Fig. 1). For this analysis, the same wave-vector decomposition as in Fig. 1 is used, with the wavevector $k_i = k_a$ incident at angle θ_a to the normal within the dielectric of refractive index n_a [the Bragg stack schematic in Fig. 2, though, is replaced by a homogeneous region with the equivalent vector diagram for a transmitted ray ($a \rightarrow b$)].

Since we are interested in slab modes with effective mode indices $\tilde{n}_a$ *below* the n_0-light-line ($\tilde{n}_a < n_0$), all slab modes are inherently leaky [27]. This is because for the former (high-index) slab $\tilde{n}_a = \beta_1/k = n_1 \sin\theta_a < n_0$, so $\theta_a < \theta_c = \sin^{-1}(n_b/n_a)$ (the critical angle) and no total internal reflection occurs, thus relying on regular (lossy) reflection. In other words, the modes must exist below the bound mode cut-off [27]. The latter (low-index) slab relies on inherently lossy Fresnel reflection for all θ_a since $n_a < n_b$. The loss characteristics are considered here only insofar as they aid the phase analysis via the Fresnel reflection coefficients [27, 28]:

$$\Gamma_{\text{TE}} = \frac{k_{ax} - k_{bx}}{k_{ax} + k_{bx}}, \quad \Gamma_{\text{TM}} = \frac{n_b^2 k_{ax} - n_a^2 k_{bx}}{n_b^2 k_{ax} + n_a^2 k_{bx}}, \tag{4}$$

which relate the incident and reflected field amplitudes, $A_{\text{TE,TM}}$ and $A'_{\text{TE,TM}}$ respectively, by $A_{\text{TE,TM}} = \Gamma_{\text{TE,TM}} A'_{\text{TE,TM}}$.

As discussed, for $\tilde{n}_a < n_0$ guidance, Snell's law implies the high-index ($n_a > n_b$) slab must have $\theta_a < \theta_c$. Since $\cos(\theta_i) = k_{ix}/k_i$ and $0 \leq \theta_a < \theta_c \leq \pi/2$ ($\Rightarrow 0 \leq \theta_b \leq \pi/2$) then $\cos(\theta_a) > \cos(\theta_b)$ and thus $k_{ax} > k_{bx}$. Equation (4) then implies $\Gamma_{\text{TE,TM}} \in \mathbb{R}^+$ so that $\text{sign}(A_{TE,TM}) = \text{sign}(A'_{TE,TM})$ and no phase shift occurs upon reflection. However, for the low-index ($n_a < n_b$) slab, $\theta_a > \theta_b$ with no critical angle threshold, so similar reasoning implies $k_{ax} < k_{bx}$. Thus $\Gamma_{\text{TE,TM}} \in \mathbb{R}^-$, meaning $\text{sign}(A_{TE,TM}) = -\text{sign}(A'_{TE,TM})$ such that a π phase shift occurs upon reflection at the interface. Note that the TE and TM modes are thus degenerate for $\tilde{n} < n_0$ due to their equivalence in this phase analysis ($\Gamma_{\text{TE,TM}}$ produce the same reflective phase conditions for both $n_a > n_b$ and $n_a < n_b$ for $\tilde{n}_a < n_0$ guidance).

The slab waveguides will only support modes, leaky or otherwise, if the accumulated transverse phase for one round-trip of the slab (traversing the slab twice upon two reflections from the interfaces) is an integer multiple of 2π. For both slabs, the transverse phase accumulated by traversing the slab region once is $k_{ax}t_a$. The forms of the low- and high-index slabs' phase relations thus differ only in their reflection terms. Equating the cumulative phase shifts to $m2\pi$ ($m \in \mathbb{Z}^+$), a dispersion relation for each waveguide is derived [27, 32]:

$$k_{ax}t_a = \begin{cases} m\pi & \text{for } n_a > n_b \text{ and } m \in \mathbb{N} \\ (m+1)\pi & \text{for } n_a < n_b \text{ and } m \in \mathbb{Z}^+ \end{cases} \tag{5}$$

where $m = 0$ is obviously not allowed for the high-index slab, implying that the $m = 0$ bound mode has no leaky counterpart [27]. By rearranging the phase relations and setting a $\rightarrow$ 1 and b $\rightarrow$ 0 for the high-index ($n_a = n_1 > n_b = n_0$) slab and a $\rightarrow$ 0 and b $\rightarrow$ 1 for the low-index ($n_a = n_0 < n_b = n_1$) slab, we find a unified dispersion relation:

$$\tilde{n}_{m_i} = \left[n_i^2 - \left(\frac{m_i \pi}{t_i k} \right)^2 \right]^{\frac{1}{2}}, \quad m_i \in \mathbb{N} \tag{6}$$

such that $m_1 = m$ and $m_0 = m + 1$. Groups of dispersion curves for a range of mode orders are plotted in Fig. 2 (right) and subsequently in Figs. 3, 4 and 5.

Here it is convenient to define that $m_1 = 0$ refers to the $\tilde{n}$-axis ($k = 0$) and $m_0 = 0$ to the n_0-light-line ($\tilde{n} = n_0$). It is easily shown that, while not representative of physical modes, these definitions still satisfy Eqs. 5 and 6. Hereon the 'SPARROW curves' will refer to both the physical slab dispersion curves ($m_{1,0} \in \mathbb{N}$) *and* these $m_{1,0} = 0$ lines, unless otherwise specified. The lower limit line $\tilde{n} = 0$ is also important but its inclusion in this set is not required, as will soon be evident.

Note that Eq. (6) is truly analytic since the non-analytic Goos-Haenchen phase shift [32] that appears in the bound-mode ($\tilde{n}_{m_1} > n_0$) solution of the high-index slab does not appear in these phase relations due to the nature of the reflective phase shifts for $\tilde{n}_{m_i} < n_0$. Also note how Eq. (6) depends only on n_i, implying that, below the n_0-light-line, the dispersion properties of each slab depend only on the slab refractive index, not that of the medium surrounding it.

Equation (6) can be arranged to give the k values of resonances of order m_i for arbitrary $\tilde{n}$ as:

$$k_{m_i} = \frac{m_i \pi}{t_i} \left[n_i^2 - \tilde{n}^2 \right]^{-\frac{1}{2}},\qquad(7)$$

where, once expressed in wavelength, it is obvious that the forms of the large-core Duguay-ARROW model (Eq. (3)) and SPARROW model (Eq. (7)) are identical save for two important differences: the SPARROW model is valid for all $\tilde{n} \leq n_0$ and depends explicitly on t_0.

3. Formal SPARROW model definition

Figure 3 (left) is produced by overlaying the slab curves (Fig. 2, right) upon the corresponding Bragg stack's bandgap map (Fig. 2, left). A clear and striking similarity between the two plots is thus revealed: each high- and low-index slab dispersion curve corresponds to a band of the bandgap spectrum. Also, the gaps completely close at the intersection points of the high and low refractive index curves (n_{m_1} and n_{m_0}, discussed further in Section 4.1). This is because $\tilde{n}_{m_1} = \tilde{n}_{m_0}$ implies optimal coupling between the two layer types so that light can easily propagate through the cladding, precluding the generation of a bandgap.
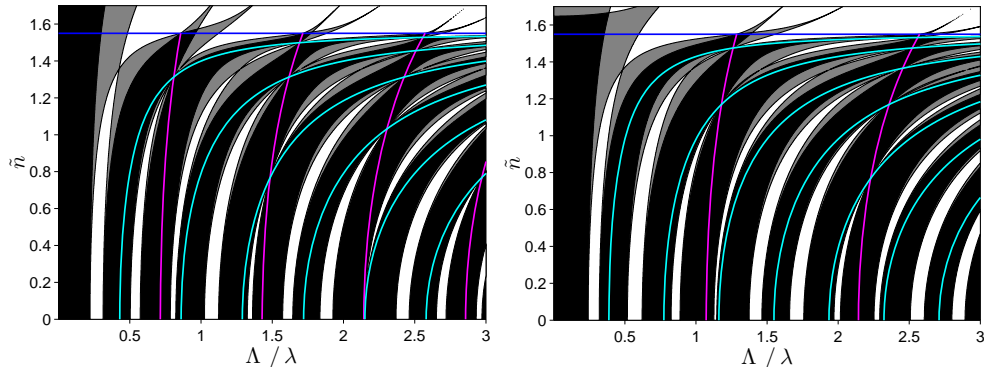

Fig. 3. **Left**: The bandgap map of Fig. 2 with the cladding layer dispersion (SPARROW) curves (Fig. 2) overlayed. **Right**: The same configuration but with the high-index layer's thickness decreased: $t_1 = 0.27\mu m \rightarrow 0.18\mu m$. The bandgap topology dramatically changes between the two cases (new bandgaps are created). Using the nomenclature and analyses of Section 4.5: $t_1 = 0.27\mu m$ produces $N_1 = 2$ and $N_2 = 4$ whereas $t_1 = 0.18\mu m$ produces $N_1 = 3$ and $N_2 = 6$.

We thus define the Stratified Planar Anti-Resonant Reflecting Optical Waveguide (SPAR-ROW) model as the use of the slab waveguides' dispersion curves (and the properties derived from them, Section 4) to quantitatively describe the resonant features of the associated bandgap spectrum. The SPARROW model thus gives direct physical insight into how the thicknesses and refractive indices of the constituent high- and low-index layers affect the resonant properties of the cladding. Our model is thus similar to the Archambault-ARROW model [9] except that the latter inseparably couples the core properties to the resonance analysis. Instead, the SPARROW model considers the effective mode index alone, with no allusion to the properties of the core itself. In this way, we have separated the cladding resonances from the core properties, giving two benefits: the ability to easily describe cladding resonances on a bandgap-style $(\Lambda/\lambda, \tilde{n})$ plot (e.g. Figs. 2,3,4 and 5); and the freedom to consider core modes of arbitrary $\tilde{n}$. The latter point requires that, for the SPARROW model to accurately predict core-mode spectral features, sensible values for a core mode's $\tilde{n}$ must be provided independently. For large-core waveguides, this is trivial, since most low-order modes will lie very close to the n_{core}-light-line (demonstrated in Section 3.1). However, it has also been shown that, at least for air-core Bragg fibers, it is possible to infer the (real part of the) core modes' $\tilde{n}$ solely from the core geometry [23, 30], including higher-order modes and small core ($\sim \lambda$) waveguides.

Note that between any two adjacent slab dispersion curves, a bandgap region exists in either the $\tilde{n}$ or k dimension, meaning that the discrete bandgaps within the stack bandgap spectrum are each *enclosed by a subset of the SPARROW curves*. We thus define the concept of a *bounding region* for any particular bandgap: the $(k, \tilde{n})$ region enclosed by the curves surrounding a particular bandgap. This behaviour implies the nontrivial discrete bandgap spectrum of the stratified cladding is replicated in position and topology by the equivalent SPARROW curves (including the physical limits $k = 0$, $\tilde{n} = 0$ and $\tilde{n} = n_0$, as discussed). Consequences and applications of this are discussed in Section 4.

3.1. *Confirmation via FEM analysis*

The validity of the SPARROW model can be verified directly by calculating the confinement loss spectrum of a particular Bragg fiber configuration in which both high- *and* low-index resonances are evident. We model a realistically achievable configuration: a fabricable (as demonstrated by Temelkuran et al. [4]) solid-cladding hollow-core Bragg fiber which is filled with a liquid of refractive index 1.45 (achievable with index-matching liquids or various oils). The cladding layers of [4] were made from As_2Se_3 chalcogenide glass ($n \approx 2.8$) and the polymer polyethersulphone (PES, $n \approx 1.55$) with thicknesses of $270nm$ and $900nm$ respectively. $n_{core} = 1.45$ is chosen here simply because it produces modes revealing interesting structure in the bandgap spectrum. We choose a smaller core diameter ($20\mu m$) than the cited fabricated fiber ($\approx 700\mu m$), and fewer rings (4 pairs of layers instead of 9), due to numerical restrictions of the method employed (the relevant discretisations are stored in finite computer memory), but note that the bandgap behaviour would be very similar between the two structures regardless (like the $700\mu m$ core, a $20\mu m$ core also produces modes close to the n_{core}-light-line, Fig. 4).

A finite element method (FEM) is used to model the modal behaviour of the waveguide via the commercial FEM package COMSOL Multiphysics. Perfectly matched layers (PMLs) [33] are employed in order to solve for the complex $\tilde{n}$, and hence for the confinement loss $CL = 20\log_{10}(e)k\text{Im}\{\tilde{n}\}$ [34].

Figure 4 shows the bandgap and CL spectra for the discussed fiber, demonstrating how the supported TE_{01} mode exists only within the cladding bandgaps, with $\tilde{n}$ having no solutions within the allowed bands, as expected. Note that the core-mode dispersion curve lies relatively close to the n_{core}-light-line for this t_{core}.

More importantly, the CL spectrum of Fig. 4 (bottom) shows how the core-mode loss dra-
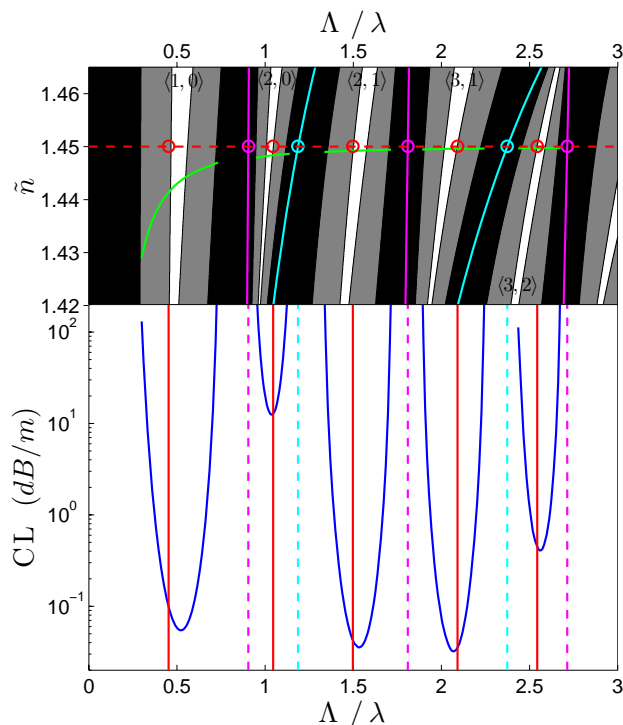
Fig. 4. **Top**: A portion of the SPARROW curves and bandgap map from Fig. 2. *Green line*: the TE_{01} mode's $Re\{\tilde{n}\}$ from the FEM calculation of the equivalent Bragg fiber, with a core of size $t_{core} = 20\mu m$. *Red dashed line*: the n_{core}-light-line ($\tilde{n} = 1.45$). *Red circles*: positions of the general antiresonance point k'_c (Section 4.2) on the n_{core}-light-line. The gaps are labelled using the nomenclature of Section 4.1. The limit value $\Lambda/\lambda = 3$ corresponds to $\lambda = 390nm$ in this case. **Bottom**: The associated CL spectrum. *Cyan and magenta dashed lines*: low- and high-index SPARROW resonances on the n_{core}-light-line, respectively (corresponding to circles of the same color in the top plot). *Red lines*: positions of the general antiresonance points from the top plot (red circles).

matically increases as the resonant features (found via the SPARROW model: $k_{m_i}(n_{core})$ via Eq. (7)) are approached. This example clearly demonstrates how the SPARROW model is required to describe the resonant properties of both high- and low-index inclusions for arbitrary $\tilde{n}$. Note how the minimum CL for each gap falls close to mid-way (in frequency) between the adjacent cladding resonance points (this important point is discussed further in Section 4.2). Of course, it is well-known that the absolute CL depends on the number of cladding layers; more layers produce a lower loss. Incidentally, the CL spectra of the next two higher-loss modes, TM_{01} and HE_{11}, have values above the domain presented in Fig. 4 (bottom), unsurprisingly (due to the narrow TM bandgap via the Brewster effect, Fig. 2) commensurate with the effectively-single-mode behaviour of Bragg fibers [3, 30].

4. Further analysis of the SPARROW model

4.1. Curve intersections and gap nomenclature

The intersection points of the high- and low-index layer dispersion curves (Eq. (6) for $i = \{1,0\}$) can be found by equating either $\tilde{n}$ or k. The intersection point of arbitrary $\tilde{n}_{m_1}(k)$ (high-index)

and $\tilde{n}_{m_0}(k)$ (low-index) curves is found to be:

$$P_{(m_1,m_0)} = (k,\tilde{n})|_{\tilde{n}_{m_1}=\tilde{n}_{m_0}} = \left(\pi \sqrt{\frac{1}{n_1^2 - n_0^2} \left(\frac{m_1^2}{t_1^2} - \frac{m_0^2}{t_0^2} \right)}, \sqrt{\frac{n_1^2 - n_0^2 \eta^2}{1 - \eta^2}} \right), \qquad (8)$$

where $\eta = \frac{m_1 t_0}{m_0 t_1}$. These points thus form the corners of the aforementioned bounding regions for a particular gap, which we shall call the *bounding points*.

Since the $\tilde{n}_{m_i}(k)$ curves monotonically approach asymptotes at n_i ($\tilde{n}_{m_i} \to n_i$ as $k \to \infty$), all gaps will have a *maximal bounding point*: the intersection point whose k and $\tilde{n}$ values are larger than those of all other bounding points for that gap, being the top-right bounding point when represented on a $(\Lambda/\lambda, \tilde{n})$ plot. Since the maximal bounding point exists for all gaps for all cladding configurations, it may be used to define a consistent nomenclature for arbitrary bandgap spectra. Here we adopt the convention that each gap is referred to by the orders of the bounding curves producing the maximal bounding point. Explicitly, an arbitrary gap is labelled as the $\langle m_1, m_0 \rangle$ gap. Some examples: the lowest order (fundamental) gap is the $\langle m_1, m_0 \rangle = \langle 1, 0 \rangle$ gap (using the Section 2.3 definition that $m_0 = 0$ corresponds to the n_0-light-line); any gap bound above by the $\tilde{n} = n_0$ line is an $\langle m_1, 0 \rangle$ gap; and so on. The gaps shown in Figs. 4 and 5 are labelled using this convention. It should be noted that this nomenclature is different (and more general) than that previously proposed by the authors in [23]; while that particular nomenclature was suitable for the particular fiber parameters examined, the system introduced here is more general and thus suitable for all possible regimes.

Using this nomenclature, we can now quantify that the portions of the $\langle m_1, m_0 \rangle$ gap that close up within the $0 < \tilde{n} < n_0$ region will do so at the intersection points $P_{(m_1,m_0)}$ and $P_{(m_1-1,m_0+1)}$, should these points exist within the domain for the given gap. If these points don't exist, the gap must then be terminated by the $\tilde{n} = 0$ or n_0 lines, leaving it open (seen explicitly in Figs. 3 and 5). Incidentally, we believe that this gap closure behaviour helps explain the mode suppression phenomena observed in [35].

4.2. The general antiresonance point

From Eq. (7) we define the general antiresonance point k_c', at arbitrary $\tilde{n} = \tilde{n}'$, as the arithmetic mean of the bounding curve values $k_{m_i}(\tilde{n}')$ either side of the gap (the central k value):

$$k_c'(\tilde{n}') = \frac{k_{m_p}(\tilde{n}') + k_{m_q}(\tilde{n}')}{2}, \qquad (9)$$

where p and q refer to the adjacent bounding curve types in the k-dimension (i.e. $p, q \in \{1, 0\}$) and m_q and m_p to their order. Note that the curves adjacent (in the k-dimension) to k_c' will change as $\tilde{n}'$ varies within the bounding region. For example, $\tilde{n}'$ in the middle section of the $\langle m_1, m_0 \rangle$ bounding region (i.e. between $P_{(m_1-1,m_0)}$ and $P_{(m_1,m_0+1)}$ in the $\tilde{n}$-dimension) implies k_c' is between curves with either $m_p = m_1$ and $m_q = m_1 - 1$ or $m_p = m_0$ and $m_q = m_0 + 1$ (depending on the type of gap), due to the monotonicity of the curves. For $\tilde{n}'$ in the top section of the bounding region (above the middle section but below $P_{(m_1,m_0)}$), k_c' will be in between curves with $m_p = m_1$ and $m_q = m_0$, whereas for $\tilde{n}'$ near the bottom of the gap (below the middle section but above $P_{(m_1-1,m_0+1)}$) k_c' is between the $m_p = m_1 - 1$ and $m_q = m_0 + 1$ curves.

Figure 4 demonstrates how k_c' naturally predicts the approximate position of lowest CL for a core mode of the fiber discussed in Section 3.1. The reason CL reaches a minimum near k_c' is that, at that point, the guided wave is maximally antiresonant with the pair of slabs producing the bounding dispersion curves (m_p and m_q); as one or the other bounding curve is approached,
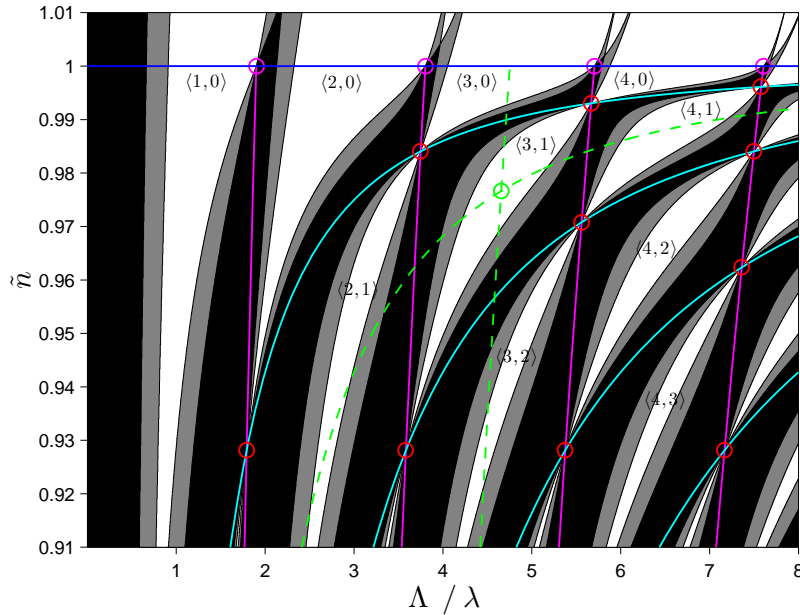
Fig. 5. SPARROW model curves overlaid upon a portion of the cladding Bandgap map of the Bragg fiber examined in [5] and [23]: $t_1 = 0.37\mu m$, $t_0 = 4.1\mu m$, $n_1 = 1.45$ and $n_0 = 1$. The color scheme is the same as for Figs. 2 and 3. The bandgaps are labelled according to the nomenclature introduced in Section 4.1. *Red circles*: intersection points (P, Section 4.1) of the SPARROW curves. *Magenta circles*: $\tilde{n} = n_0$ resonances (Eqs. 3 and 7). *Green dashed curves*: a specific bandgap's half-order curves, the intersection of which form P_c (Section 4.4), the *green circle*. The chosen gap is of order $\langle m_1, m_0 \rangle = \langle 3, 1 \rangle$ with $P_c = (k_c, \tilde{n}_c) \approx (5.34898\mu m^{-1}, 0.976641)$.

the wave becomes more resonant with the associated slab, thus allowing greater coupling from the core to the cladding. This is why the resonances of all layer types must be considered *together*, rather than separately, as discussed earlier, and is inherent in the definition of k'_c. The general antiresonance point is thus a powerful tool for waveguide design and analysis, allowing immediate determination of the approximate point of minimum CL at arbitrary $\tilde{n}$ within an arbitrary bandgap.

Note that, due to the analyticity of Eq. (9), the derivatives of k'_c with respect to all waveguide parameters ($\partial k'_c / \partial n_i$, $\partial k'_c / \partial t_i$, etc.) can be easily derived, but are omitted here for brevity. These derivatives are ideal for the direct calculation of fabrication tolerances in waveguide design, or sensitivities to core materials for sensing, for example.

4.3. Special cases

There are two important special cases of the SPARROW model: $\tilde{n} = n_0$ and $\tilde{n} = 0$. It is easily shown that the former actually reduces to the large-core limit of the Duguay-ARROW model, since by setting $i = 1$ and $\tilde{n}_{m_1} = n_0$ in Eq. (6) we derive Eq. (3). These $\tilde{n} = n_0$ resonances are shown in Fig. 5 (magenta circles). Thus, the SPARROW model also explains why the Duguay-ARROW model in the large-core regime (Litchinitser et al. [20]) is typically independent of the thickness of the low-index region: all orders of the low-index slab dispersion curves ($\tilde{n}_{m_0}$) have an asymptote at $\tilde{n} = n_0$ and hence never intercept it; their resonant features can never appear on the n_0-light-line (the region of applicability of Eq. (3)).

The other special case, $\tilde{n} = 0$ (the zero-line), is derived in much the same way. However, in this case, both high- and low-index curves intercept the zero-line. Setting $\tilde{n}_i = 0$ we derive:

$$\lambda_{m_i} = \frac{2n_i t_i}{m_i} \tag{10}$$

where $i \in \{1,0\}$. $\tilde{n} = 0$ corresponds to rays normally incident to the layered cladding, similar to high-order modes within hollow-core solid-cladding Bragg fibers [30] which lie within $0 < \tilde{n} \leq 1$.

While useful in themselves, these two special cases reveal important information about the structure and topology of the Bandgap map, discussed in more detail in Section 4.5.

4.4. The central gap point

The concept of a central gap point can now be introduced. Note that the slab dispersion curves with half-orders ($\frac{1}{2}, \frac{3}{2}, \frac{5}{2}, \ldots$) fall mid-way between adjacent integer-order curves for both $i = \{1,0\}$ (when expressed in terms of k and $\tilde{n}$). An example is shown in Fig. 5 (green dotted curves). Thus, we define the *central gap point* as the intersection point of the half-order curves within a particular gap. In the nomenclature defined in Section 4.1, the curves producing the central gap point for the $\langle m_1, m_0 \rangle$ gap are the $m'_1 = m_1 - \frac{1}{2}$ and $m'_0 = m_0 + \frac{1}{2}$ curves, so that the position of the gap's center is given a modified form of Eq. (8) where $m_1 \rightarrow m_1 - \frac{1}{2}$ and $m_0 \rightarrow m_0 + \frac{1}{2}$, namely:

$$P_c = (k_c, \tilde{n}_c) = P_{(m_1 - \frac{1}{2}, m_0 + \frac{1}{2})} = \left(\pi \sqrt{\frac{1}{n_1^2 - n_0^2} \left[\left(\frac{m_1 - \frac{1}{2}}{t_1} \right)^2 - \left(\frac{m_0 + \frac{1}{2}}{t_0} \right)^2 \right]}, \sqrt{\frac{n_1^2 - n_0^2 \eta_c^2}{1 - \eta_c^2}} \right), \tag{11}$$

where $\eta_c = \frac{(m_1 - \frac{1}{2}) t_0}{(m_0 + \frac{1}{2}) t_1}$. In fact it can be shown that P_c is entirely commensurate with the general antiresonance point (k'_c) of Eq. (9) such that:

$$k'_c(\tilde{n}_c) = k_c. \tag{12}$$

The proof for this is omitted for brevity, but only requires some careful manipulation and a demonstration that $\tilde{n}_c$ always lies between the middle two intersection points $P_{(m_1+1, m_0)}$ and $P_{(m_1, m_0-1)}$ so that k'_c is always bound on either side by either the $m_p = m_1$ and $m_q = m_1 - 1$ curves or the $m_p = m_0$ and $m_q = m_0 + 1$ curves (as discussed in Section 4.2). An example based on the fiber cladding examined in [5, 23] is shown in Fig. 5 (green circle), where $P_c = P_{(\frac{5}{2}, \frac{3}{2})} \approx (5.34898 \mu m^{-1}, 0.976641)$ corresponding to the $\langle 3,1 \rangle$ gap.

Since the gaps bound by the $\tilde{n} = n_0$ and/or $\tilde{n} = 0$ lines are open (above and below, respectively), this definition of the center point is insufficient when P_c reaches these lines, or where P_c simply doesn't exist (as is the case for all $\langle m_1, 0 \rangle$ gaps). In these cases, we use the general antiresonance point (Eq. (9)) to define $P_c = (k'_c(\tilde{n}'), \tilde{n}')$ where $\tilde{n}' = n_0$ or 0 as appropriate. Thanks to Eq. (12), this gap center formalism is thus consistent for all bandgaps.

It is expected that P_c will determine the approximate point of lowest modal CL for a given bandgap in not just the k-dimension (via the relation to k'_c from Eq. (12)) but also the $\tilde{n}$-dimension. This is to be expected from the work of [30], where it was demonstrated that as the bandgap edges are approached from any direction, CL generally increases. Since P_c dictates the point at which light is maximally antiresonant with both cladding layer types, it is reasonable to expect that the CL is thus minimum near this point. While omitted here for brevity, a quantitative verification of this would be straight-forward, requiring the CL spectra of the modes of

interest to be calculated for a range of $\tilde{n}$. This could be achieved by iterating the spectral analysis (via a FEM as in Section 3.1, for example) over a range of n_{core} to generate modes within the entire domain of the bandgap of interest (i.e. to calculate CL in both the k- and $\tilde{n}$-dimensions).

Also, similar to the discussion of Section 4.2, the derivatives of P_c with respect to all cladding parameters ($\partial k_c/\partial n_i$, $\partial k_c/\partial t_i$, $\partial \tilde{n}_c/\partial n_i$ and $\partial \tilde{n}_c/\partial t_i$) can also be easily derived, and would also be ideal for similar applications.

4.5. Bandgap topology and the bounding region

Here we derive another powerful feature of the SPARROW model. Equation (8) can be used to determine the number of bandgaps (or more precisely, bounding regions) that exist between a pair of adjacent high-index slab curves, $n_{m_1}(k)$, which have orders $m_1 - 1$ (left curve in the k-dimension) and m_1 (right curve). We define D_{m_1} as the domain enclosed by this curve pair and the $\tilde{n} = n_0$ and $\tilde{n} = 0$ lines. We focus on the TE bandgaps here, since the TM gaps have the same topology save for the simple gap closure induced by the Brewster effect (Section 2.1, Figs. 2 and 3).

It is easy to see (e.g. Figs. 2 and 3) that the number of bounding regions, hence TE gaps, within D_{m_1} is one greater than the number of intersection points made by the low-index curves [$n_{m_0}(k)$] with the rightmost bounding curve [$n_{m_1}(k)$], excluding the n_0-light-line ($m_0 = 0$). To show this analytically, we must enforce upon the intersection point expression (Eq. (8)) the physical condition: $P_{(m_1,m_0)} \in \mathbb{R}^2$. By enforcing $k \in \mathbb{R}$, the square-root requires $(m_1/t_1)^2 - (m_0/t_0)^2 > 0 \Rightarrow \eta > 1$ (where η is defined with Eq. (8)). This can be used to find an upper limit $m_0 < m_1(t_0/t_1)$, but a more strict limit is found by enforcing the second physical condition $\tilde{n} \in \mathbb{R}$: since $\eta > 1$, $1 - \eta^2 < 1$ so that the numerator (within the square-root) must also be negative: $n_1^2 - n_0^2\eta^2 < 1 \Rightarrow n_1/n_0 < \eta$. This last inequality gives the most strict range physically imposed on m_0, namely:

$$m_0 < m_1 \frac{n_0 t_0}{n_1 t_1}. \tag{13}$$

Thus, the maximum permissible order of an m_0-curve within D_{m_1} is:

$$m_0^{\text{max}} = \text{floor}\left\{m_1 \frac{n_0 t_0}{n_1 t_1}\right\}, \tag{14}$$

which is also the number of m_0-curves within D_{m_1} (excluding the $\tilde{n} = \{0, n_0\}$ lines). The number of TE bandgaps within D_{m_1} is thus $m_0^{\text{max}} + 1$; the '+1' accounting for the ever present $\langle m_1, 0 \rangle$ gaps, bound above by the n_0-light-line, whose maximal bounding point $P_{(m_1,0)}$ doesn't contribute to m_0^{max} by definition, as discussed.

There is an exception to this analysis: where a maximal bounding point lies *on* the zero-line ($\tilde{n} = 0$) such that the point exists but the associated gap does not (the bounding region becomes singular). In this case, the number of gaps within D_{m_1} is exactly equal to the number of intersection points on $\tilde{n}_{m_1}(k)$ (including the $\tilde{n} = 0$ bounding point). Quantitatively, the condition for this behaviour can be deduced from the SPARROW model's $\tilde{n} = 0$ special case (Eq. (10)) by setting $\lambda_{m_1} = \lambda_{m_0}$, demonstrating that the above inequality (Eq. (13)) becomes an *equality* (i.e. the floor function of Eq. (14) becomes redundant).

We can thus express the total number of gaps bound within D_{m_1} as:

$$N_{m_1} = \begin{cases} m_0^{\text{max}} + 1 & \text{when } m_0^{\text{max}} < m_1 \frac{t_0 n_0}{t_1 n_1} \\ m_0^{\text{max}} & \text{when } m_0^{\text{max}} = m_1 \frac{t_0 n_0}{t_1 n_1} \end{cases} \tag{15}$$

which depends only upon the cladding parameters and just one order parameter, m_1 (required to define D_{m_1}).

The only difference in topology for the TM gaps over the TE gaps is that the Brewster-induced gap closure increases the number of gaps within D_{m_1} by 1 (i.e. $N_{m_1} + 1$), the position of the extra closure being $\tilde{n} = n_B$ (Section 2.1). The only exception is when n_B coincides with a TE gap closure point, $P_{(m_1,m_0)}$, in which case the associated TM gap's bounding region becomes singular (similar to the P_c at $\tilde{n} = 0$ case above) and the number of gaps within D_{m_1} is identical to the TE case (i.e. N_{m_1}).

The above expressions for the intersections points (Eq. (8)) and the number of gaps within a given domain D_{m_1} (Eq. (15)) explicitly define the topology for any given bandgap spectrum: the number of gaps (in a finite domain) and how they join together. Figure 3 gives an explicit example of how a bandgap spectrum topology can change with varying cladding parameters.

5.   Concluding remarks

In this work we have demonstrated an intimate relationship between the bandgap and antiresonance pictures of light confinement in binary-layered-cladding waveguides on and *below* the low-cladding-index light-line, implying that Bragg fibers and integrated-ARROWs guide by fundamentally the same principles. This was done by developing an antiresonance model, the SPARROW model, which describes the resonances of an arbitrary waveguide's cladding layers, independent of the core properties. The SPARROW model is a generalisation of the Archambault-ARROW model [9] in that we consider only the resonant properties of the cladding layers and not that of the core, permitting the direct comparison of the layers' dispersive behaviour with the associated Bloch-wave bandgap spectra. Foremost, the model demonstrates that the cladding layer dispersion curves replicate the nontrivial structure and topology of the analogous 2-D Bloch-mode bandgap spectrum. By exploiting this, the model is also capable of quantitatively and analytically describing nontrivial features of such spectra. Among the most important features of the model derived were: a consistent nomenclature for arbitrary bandgap spectra ($\langle m_1, m_0 \rangle$); the approximate position of lowest core-mode confinement loss of any gap via the general antiresonance point (k_c'); the precise closure points of a given gap ($P_{(m_1,m_0)}$ and/or $P_{(m_1-1,m_0+1)}$); the center of a gap in both $\tilde{n}$- and k-dimensions via the central gap point (P_c); and the number of bandgaps within a specific domain (e.g. N_{m_1} for TE), thus the bandgap spectrum topology; all via simple analytic expressions.

The SPARROW model is thus a powerful and simple tool for the spectral analysis and design of layered cladding dielectric waveguides with core refractive indices equal to or less than the lowest cladding index. Integrated-ARROWs have recently been demonstrated as ideal hollow-core waveguides for sensing and microfluidics [13]. However, our analysis of a liquid-core solid-cladding Bragg fiber implies that fibers have similar promise. These principles are also useful for achieving guidance in nonlinear liquids and gases, important for the development of novel nonlinear waveguides.